

High speed motion generated by an oscillating microfiber

By

He(Rick) Qi

B.S., Zhejiang University, 2008

Thesis

Submitted in partial fulfillment of the requirements for the
Degree of Master of Science in the Department of Engineering at Brown University

PROVIDENCE, RHODE ISLAND

MAY 2010

This thesis by He(Rick) Qi is accepted in its present form
by the Brown University Department of Engineering as satisfying the
thesis requirements for the degree of Master of Science.

Date _____

Kenny Breuer, Advisor

Approved by the Graduate Council

Date _____

Sheila Bonde, Dean of the Graduate School

Vita

He(Rick) Qi was born in Guangzhou, China, on 21 May 1986, to Daihua Yang and Yong Qi. Rick graduated with honors of his Guangdong Experimental High School (Guangzhou, China) class in June 2004. He then attended Zhejiang University in Hangzhou, China where he studied Mechanical Engineering and received his Bachelor of Science degree in June 2008. Rick is currently finishing his Master of Science degree requirements in the Department of Engineering at Brown University.

Preface & Acknowledgement

My foremost thank you goes to my advisor, Dr. Kenneth Breuer, for his continuous guidance and invaluable engineering and research experience. Also, for his patience and passion, I am grateful.

I thank Dr. Shane Woody from Insitutec, for his generosity in providing experiment equipments.

My graduate program is supported by Zhejiang University, Chinese Scholarship Council and Brown University. I thank them.

The work present in throughout this paper is under the guidance of Dr. Bian Qian of Microfluidics Lab of Brown University. His enormous experience and passion in research have motivated me along the road. Without him, I cannot finish this project. I thank him for that.

Thank you to the members of Kenny Breuer's Lab for generating a fun and creative work environment. Members include: Bian Qian, John DiBenedetto, Jun Kudo, David Gagnon, Charles Peguero, Arnold Song, Rye Waldman and Adam Hoffman. The time we hanged out will certainly be missed.

I thank my friend Qian Zhu for her unconditional and long-time support and Dr. Jianzhong Zhang for his help in advancing my tennis skills and guiding me through hard times.

I thank my grandparents, parents, and cousins for their tireless and unconditional love and support.

Table of Contents

VITA.....	III
PREFACE & ACKNOWLEDGEMENT.....	IV
TABLE OF CONTENTS.....	V
LIST OF FIGURES.....	VII
LIST OF SYMBOLS.....	XII
1. ABSTRACT.....	XIII
2. INTRODUCTION AND BACKGROUND.....	1
2.1 Experimental observations.....	1
2.2 Theoretical analysis.....	6
3. EXPERIMENTAL SETUP AND PROCEDURE.....	10
3.1 The overall setup.....	10
3.2 Mechanical design.....	11
3.3 Control system.....	15
3.4 Particle Tracking Velocimetry (PTV).....	16
3.4.1 Advantages of PTV.....	16
3.4.2 Principles of PTV.....	17
3.4.3 Choose seed particles.....	19
3.4.4 Tracking uncertainties.....	21
3.5 Experiment procedure and data summarized.....	22
4. RESULTS AND DISCUSSION.....	25
4.1 Calibration.....	25

4.2 2-D Flow field.....	30
4.3 3-D Flow field.....	32
4.4 Amplitude effects	35
4.4.1 Energy versus Reynolds number	35
4.4.2 Streamlines versus Reynolds number	40
4.4.3 Distance effect	44
5. CONCLUSION AND FUTURE STUDY	46

List of Figures

Figure 1: Vortex system formed by vibrating air round a cylinder. Cylinder diameter is 0.475cm and air is driven by a loud speaker. [3]	2
Figure 2: MgO particles in the oscillating air. Circular cylinder is photographed from above. Radius of the cylinder is 0.11 cm, frequency of oscillation is 200Hz, temperature of air is 20°C and exposure time is 1/20 second. [1]	3
Figure 3: Frequency dependence of predicted (Upper) and measured (Lower) reagent concentrations. Eddies function as a microchemical trap. Because the electrode eddies are hydrodynamically isolated from the bulk fluid, chemicals added to the eddies can escape only by slow molecular diffusion (mass-transfer-limited dosing). Experimental concentration images were acquired by using imaging Raman spectroscopy in 25 mM ferricyanide and ferrocyanide solution supported with 1 M NaOH. An illumination shadow does not allow imaging behind the electrode. [8]	4
Figure 4: Schematic of the flow channel and flow symmetry planes. Each plane was illuminated in turn through transparent channel walls using a line-focused laser beam (left). Schematic of representative streamlines for 3-D steady streaming within one channel quadrant. Planes B and C define two quadrant boundaries, and the full cylinder length (channel height) is shown. Streamlines near the cylinder middle represent the 2-D eddy formed within the channel core. The lower flow represents the junction streaming formed near the cylinder ends (right). [9]	5
Figure 5: The flow with a microvortex on the right is generated by a sharp edge. Movie images show 3-D recirculating flow by a nonsharp edge on the left. [10]	6

Figure 6: The phase lag between the radial and the tangential velocity. It is obtained from the zeroth approximation. [1]..... 8

Figure 7: Streamlines of the stationary flow in one quadrant. The streamline is obtained from the first order approximation. The radius of the cylinder $a=0.11\text{cm}$ and the radius of the outer boundary $R=20*a$. [1] 9

Figure 8: Experimental setup 1, tuning fork, oscillating fiber, microscopy and video/image taking system. 2, Photron APX RS high speed camera. 3, Nikon TE200 inverted fluorescence microscopy..... 11

Figure 9: The “Quater Research and Development” micropositioner has a resolution of 0.01 mm per marking on the micrometers and travel range 0.5” on X, Y, Z directions. The “Thorlab” goniometer has a resolution of 0.167° and ranges of $\pm 15^\circ$ and $\pm 10^\circ$ at two rotational axes respectively. The micropositioner is used to move stage in X-, Y- and Z- directions and goniometer is used to make sure the probe (fiber) is vertically placed... 12

Figure 10: The front view of goniometer setup. The whole setup is placed on the micro stage of microscopy. The micro stage itself can move too. 13

Figure 11: Oscillating fiber and its driven system. The fiber is attached to a tuning fork which is controlled by the probe amplifier and oscillates at 32 kHz..... 13

Figure 12: The actual image of standing wave fiber. The total length is 1mm and the distance from the tip to the first node is $270\mu\text{m}$ 14

Figure 13: Adjust tip inclination. Image of the tip and the top are overlapped in one image. If we know the length of fiber, we are able to calculate the inclination angle. 15

Figure 14: Schematic of the control system. Fast camera, image intensifier and micro stage are all connected to computer via NIDAQ card. They can be all controlled by a single Matlab file, which reduces a large amount of manual work. 15

Figure 15: Basic principles of PTV. The velocity (speed and direction) is obtained by dividing the distance between two indentified particles in two subsequent frames by the time interval between the frames. 17

Figure 16: Comparison of PIV and PTV images. This is an ideal PTV image taken by our experimental setup. The distance among each particle is larger than its displacement between two frames. Also the particle light intensity is strong contrast to the background. They can be easily identified. 19

Figure 17: Particle center locating principle. Through Gaussian fit at X and Y axis, we identify the center (X_0 and Y_0) of particle with sub micron precision. The distribution shown in the figure is the theoretical intensity distribution. A is a constant here. 21

Figure 18: Tip oscillating images in water. The fiber material is glass and the solution is water. Driven voltage starts from 0V to 2.5V. Images are taken by IDT camera. 25

Figure 19: Image processing for tip amplitude. 26

Figure 20: Tip oscillating center shifts as the amplitude increases. D is the tip diameter and Y_0 , X_0 are the beginning locations. 27

Figure 21: Length of short axis vs. driven voltage. D is the tip diameter and L is the actual length of short axis. 28

Figure 22: Viscosity of water and glycerol solution. X-axis is the weight percentage of glycerol in solution. 28

Figure 23: Amplitude vs. driven voltage. Blue, red and green means water, 34% glycerol and 65% glycerol solution respectively. V_{rms} means the root mean square velocity. Under different percentage of glycerol and water mixture, the amplitude changes significantly. But they all remain linear. 29

Figure 24: video processing results--Streamlines and contours for horizontal velocities. The tip is placed $10\mu m$ above the substrate, oscillating along X-axis with $1.38\mu m$ amplitude. The Reynolds number is 0.25. Red means flow goes to the positive side of the axis and blue means flow goes to the negative side of the axis. 30

Figure 25: Processing images of different flow layers. The left one shows how focal plane moves up by $3\mu m$ each time and records videos. The right one quantitatively shows the image processing results of multi-layer video recording and tells us how the horizontal velocities increase from the substrate. ($Re=0.25$) 31

Figure 26: 3-D streamlines. (1), top view, the streamlines in the green rectangular box is shown in 3-D in the rest of the plots; (2), 3-D view of streamlines and W velocity contour; (3), U velocity contour; (4), V velocity contour. ($Re=0.25$) 33

Figure 27: Velocity vector cross-section manifestation. The left one is on the plane parallel with X at $y=0$, the right one is parallel with Y at $x=0$. Red means the flow is going up and blue means the flow is going down. ($Re=0.25$) 34

Figure 28: Calculating the energy. The red circle in left figure shows where we interpolate the surrounding fluid to get the flow field energy. The right figure tells we calculate the flow field energy at different heights. 35

Figure 29: Energy versus height under four different Reynolds numbers. 36

Figure 30: Normalized energy versus height under four different Reynolds numbers....	36
Figure 31: Energy based on different radii. We defined circles with different radii surrounding the tip. By interpolating velocities u , v and w on the circle, we can calculate the flow field energy. The black dot in the center represents the tip of the oscillating fiber.....	37
Figure 32: Energy decay from the center for four different Reynolds numbers.....	37
Figure 33: Horizontal energy versus vertical energy obtained at the case $Re=0.25$. It is taken at the height where the tip is. D is the diameter and R is the radius of the tip.	38
Figure 34: Energy integrated by volume. We sum all the velocities lying on the volume of the cylinder by different radii (red, black, green and dark), from the height $z=0$ to $z=24\mu m$. The cylinders radius increase from $r/D=2$ to $r/D=6$, where D is the diameter of the tip. The black column in the middle represents the fiber.....	39
Figure 35: Energy integrated by volume.....	39
Figure 36: Results of the energy integrated on surface. The radius increases from $r/R=2$ to $r/R=12$	40
Figure 37: Flow fields transform as the Reynolds number changes.	41
Figure 38: Tangential velocity decays along the center. Tangential velocities are interpolated on the red and black straight line. $Re=0.98$ (above). $Re=0.04$ (below).	43
Figure 39: Energy decays from the center for the case $Re=0.04$	44
Figure 40: Pumping & boundary effect. Tip is placed above substrate $10\mu m$ or $20\mu m$. The Y-axis shows the number of particles per frame at time t divided by the number of particles at the initial frame.....	45

List of symbols

A , amplitude

a & R , radius

D , diameter

t & T , time

u & U , velocity

ω , frequency

η , kinematic viscosity

Re , Reynolds number

ψ , streamline function

ρ , density

σ_u , root-mean-square error in the velocity measurement

$\sigma_{\Delta x}$, root-mean-square error in displacement measurement

d_e , diameter of diffracted particle image

d_r , resolution of recording medium

d_p , the tracer particle diameter

M_0 , image magnification

λ , the wave length of illumination light

$f^\#$, f-number

1. Abstract

Since the introduction of the first microfluidic device, manipulating fluid in micron or even nano scales has captured increasing attention. Investigation into its application in biotechnology has been the most intense. Such applications include immunosensors, reagent mixing, content sorting and drug delivery. Microfluidic devices are preferable to conventional technology because they require few samples and produce rapid results. This thesis carefully studies the flow phenomena caused by a high frequency oscillating micro fiber, which is potentially available for mixing on microfluidic devices. The oscillation induces 3-D steady streaming which has not been studied nearly as thoroughly as its 2-D counterpart. In this experiment, strong three dimensional steady streaming is observed. By changing the viscosity and driven amplitude, we can control the Reynolds numbers and have different flow phenomena. After applying Particle Tracking Velocimetry (PTV), we carefully measure this three dimensional flow from the perspectives of strength of Z-direction flow, energy distribution, transition of the flow pattern and tangential and radial flow speed. My results show similarities and differences to previous 2-D steady streaming results.

2. Introduction and Background

2.1 Experimental observations

Steady streaming is one kind of time-averaged flow effect. Usually the fluctuating flow results in a nonzero mean. According to Holtmark, streaming effects in flow were first discovered by the great experimentalist Michael Faraday in 1831 [1], the same year he discovered that magnetic fields can induce electricity. There are two main types of streaming effects. The first, which we will discuss in this thesis, is associated with energy dissipation within the Stokes boundary layer adjacent to a solid boundary when the oscillating flow is interacting with the solid surface. The second one usually happens when a sound wave propagates through an unlimited volume of fluid. More commonly known as “quartz wind”, it is named for the wind observed to blow away from oscillating quartz crystals. Because the intensity of quartz wind decays quickly along the direction it propagates and the energy it carries is too small [2], we are generally not interested in applying the effect to microfluidic devices. In our study, we focus on the first kind of steady streaming effect.

The earliest demonstration of steady streaming we can find is given by Andrade *et al.* in 1931 [3]. He vibrated the air around a cylinder tube at diameters between 1mm and 5mm, using smoke particles as tracers. This can be shown by Figure 1. The streaming flow was induced by the interaction between the main fluid body and the non-slip boundary. We can clearly see the outer vortex while the inner vortex is a little bit obscure.

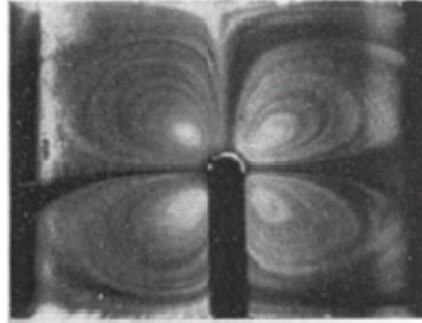


Figure 1: Vortex system formed by vibrating air round a cylinder. Cylinder diameter is 0.475cm and air is driven by a loud speaker. [3]

Unlike Andrade who made no quantitative analysis, Holtsmark *et al.* [1] performed a carefully designed experiment based on his numerical analysis. He placed a cylindrical obstacle with a diameter of 0.11cm at the antinode of a Kundt's tube. MgO was used as tracer particles (Figure 2). All images were taken through an objective placed above the Kundt's tube. Holtsmark observed that the thickness of the boundary layer is a function of $D\left(\frac{\omega}{\eta}\right)^{1/2}$ and decreases as $D\left(\frac{\omega}{\eta}\right)^{1/2}$ increases. Here D is the diameter of the cylinder, ω is the frequency and η is the kinematic viscosity.

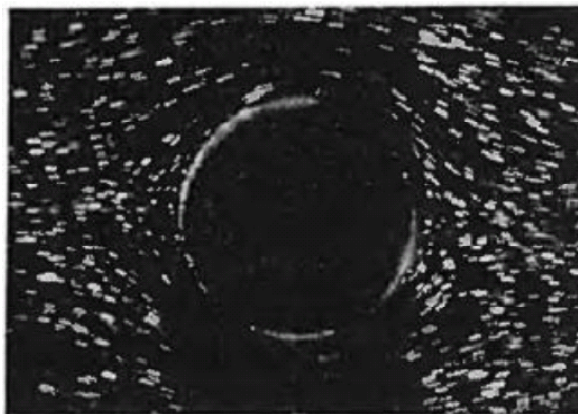


Figure 2: MgO particles in the oscillating air. Circular cylinder is photographed from above. Radius of the cylinder is 0.11 cm, frequency of oscillation is 200Hz, temperature of air is 20°C and exposure time is 1/20 second. [1]

In recent years, people are most interested in applying streaming effects to microfluidics control. Rife *et al.* [4] used quartz wind type streaming to propel fluid. Due to the low back pressure (about 0.15Pa), “quartz wind” type pressure driven flow is only competitive in low-impedance flow or closed-loop flow. Also, heating may ultimately limit the intensity. Yang *et al.* [5] employed acoustic vibration generated by piezoelectric ceramic to actively mix water and fluorescent dye in a 6mm×6mm×0.06mm chamber. Sritharan *et al.* [6] also did an acoustic mixing experiment in a micro channel 75μm high and 100μm wide and he was able to observe different mixing fractions under different amplitudes.

Beyond the “quartz wind” type acoustic streaming, there are more efforts to study boundary induced type steady streaming. The first reason is because its amplitude is independent of fluid viscosity. As shown by Squires *et al.* [7], the steady inertial force is balanced by steady viscous forces, so the streaming velocity is independent of viscosity. The velocity scale for steady boundary-driven streaming is

$$U_s \sim \frac{U_0^2}{\omega L} \quad (1)$$

Here U_0 is the amplitude of oscillating flow, ω is frequency and L is characteristic length. Thus the streaming effects are much stronger than the quartz wind type. Second, heat and bubble generation is not associated with the streaming. A group at the University of

Washington led by Professor Daniel Schwartz has used streaming induced stokes layers to trap high concentration chemical reagents at a scale smaller than $500\mu\text{m}$ (Figure 3) [8].

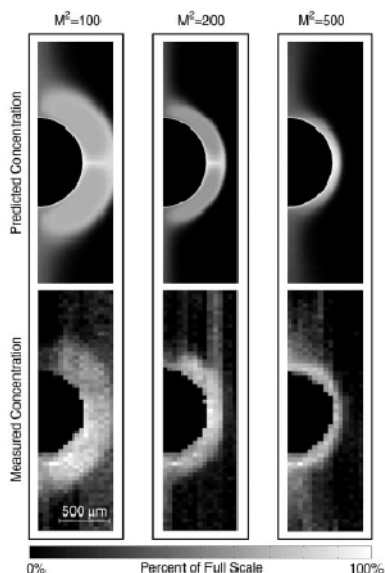


Figure 3: Frequency dependence of predicted (Upper) and measured (Lower) reagent concentrations. Eddies function as a microchemical trap. Because the electrode eddies are hydrodynamically isolated from the bulk fluid, chemicals added to the eddies can escape only by slow molecular diffusion (mass-transfer-limited dosing). Experimental concentration images were acquired by using imaging Raman spectroscopy in 25 mM ferricyanide and ferrocyanide solution supported with 1 M NaOH. An illumination shadow does not allow imaging behind the electrode. [8]

In 2005, they did another carefully designed experiment which was able to visualize the 3-D steady streaming flow at sub millimeter scale [9]. The experiment setup is shown in Figure 4. Here, polystyrene microspheres were seed particles and the flow was oscillated by a piezoelectric diaphragm.

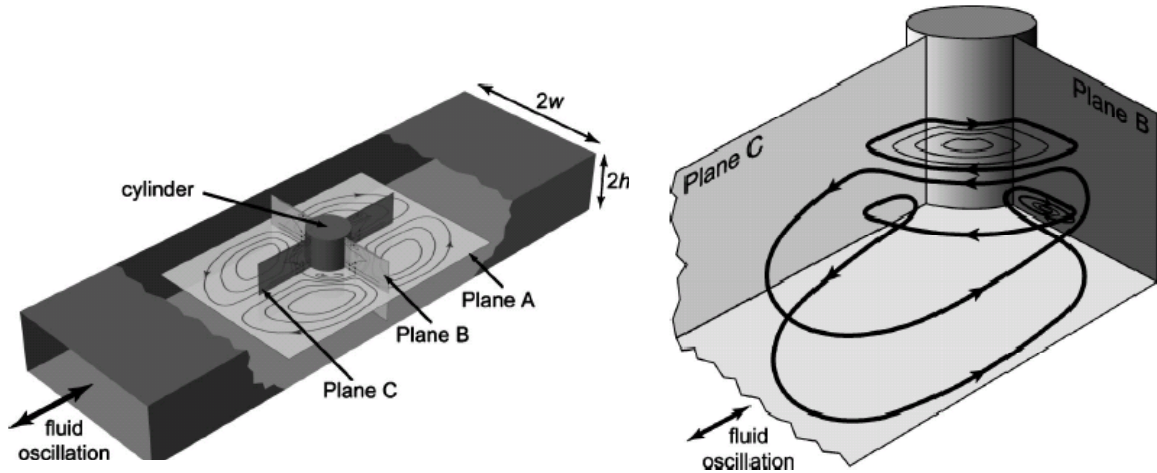


Figure 4: Schematic of the flow channel and flow symmetry planes. Each plane was illuminated in turn through transparent channel walls using a line-focused laser beam (left). Schematic of representative streamlines for 3-D steady streaming within one channel quadrant. Planes B and C define two quadrant boundaries, and the full cylinder length (channel height) is shown. Streamlines near the cylinder middle represent the 2-D eddy formed within the channel core. The lower flow represents the junction streaming formed near the cylinder ends (right). [9]

A group in Taiwan also visualized the 3-D nature of steady streaming under their designed environment [10]. They actuated a micro plate ($100 \times 100 \times 1.2 \mu\text{m}^3$) by Lorentz force. The generated microvortices were about $100 \mu\text{m}$ in diameter. They found the sharpness of the edge of the micro plate played a crucial role in the formation of streaming flow because sharp edge induced flow detachment (Figure 5).

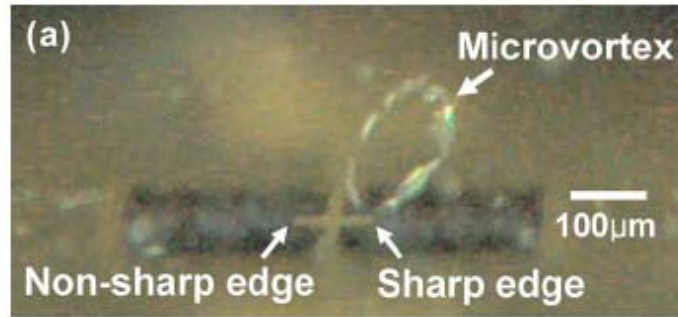


Figure 5: The flow with a microvortex on the right is generated by a sharp edge. Movie images show 3-D recirculating flow by a nonsharp edge on the left. [10]

2.2 Theoretical analysis

The first theoretical work on steady streaming (which was called “acoustic streaming” at that time) should be attributed to Rayleigh in 1883. In his book, “Theory of Sound” [11], he studied the standing sound wave between plane walls. He also pointed out that acoustic streaming, which requires the solution of the hydrodynamic equations of higher degree, was different from elementary treatment of sound [12].

Rayleigh explained acoustic streaming intuitively, but not until Eckart *et al.* [2] were people able to give out a solution for second order viscous force. He started with an inviscid fluid,

$$\frac{\partial \rho}{\partial t} + \nabla \cdot (\rho u) = 0 \quad (2)$$

$$\frac{\partial(\rho u)}{\partial t} + \rho u \cdot \nabla u + u \nabla \cdot (\rho u) = -\nabla p \quad (3)$$

He then applied the perturbation method, writing the density and velocity as

$$\rho = \rho_0 + N\rho_1 + N^2\rho_2 \dots \quad (4)$$

$$u = u_0 + Nu_1 + N^2u_2 \dots \quad (5)$$

N is defined

$$N = \frac{UT}{X} \quad (6)$$

U (velocity), T (time) and X (length) are chosen to represent different problems.

$N \ll 1, N \sim 1, N \gg 1$.

After adding back the viscous term, acoustic energy conservation condition and boundary conditions (a long tube with rigid walls and both ends permit an axial sound beam to enter and leave the tube without reflection), he found that the wind speed in any given fluid depends on the bulk viscosity coefficient μ' of that fluid.

Based on the earlier work of Eckart *et al.* [2] and Nyborg *et al.* [13], Holtsmark *et al.* [1] studied boundary-induced type streaming and gave a semi-numerical analysis. He considered an oscillating motion in a viscous fluid surrounding a circular cylinder with radius a and axis normal to the x, y plane and passing through the origin. He interpreted the problem in two parts: flow in the viscous boundary layer $\psi_2^{(0)}$ and flow outside the boundary layer $\psi_1^{(0)}$ which represents a potential laminar flow field.

$$\nabla^2 \psi_2^{(0)} = 0 \quad (7)$$

$$\left(\nabla^2 - \frac{1}{\eta} \frac{\partial}{\partial t} \right) \psi_2^{(0)} = 0 \quad (8)$$

$$\psi^{(0)} = \psi_1^{(0)} + \psi_2^{(0)} \quad (9)$$

Here η is the kinematic viscosity. After applying the boundary conditions (like no-slip boundary condition at rigid walls and oscillating flow field), Holtsmark used a semi-numerical method to solve the Hankel functions and phase lag (Figure 6) between the

radial velocities and tangential velocities near the cylinder wall which caused the elliptical motion of fluid elements.

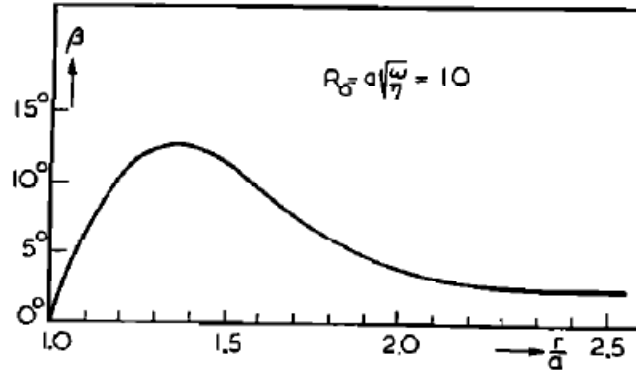


Figure 6: The phase lag between the radial and the tangential velocity. It is obtained from the zeroth approximation. [1]

Here $R_0 = a\left(\frac{\omega}{\nu}\right)^{\frac{1}{2}} = 10$. With a similar successive approximation like Eckart *et al.* [2],

$$\psi = \psi^{(0)} + \psi^{(1)} + \psi^{(2)} + \dots \quad (10)$$

The first approximation gives a stationary circulation with symmetry of $\sin 2\theta$, so we have elliptical orbits at every quadrant near the cylinder. The second approximation does not contribute anything to the stationary flow but indicates the thickness of the inner vortices.

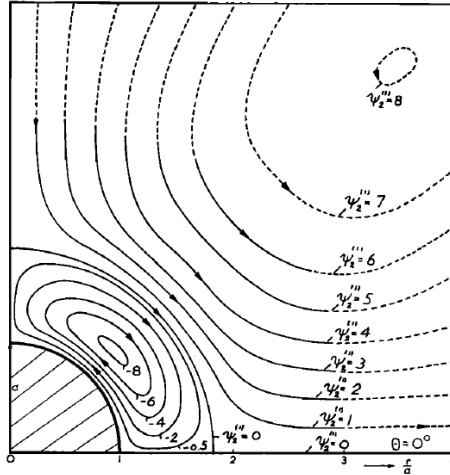


Figure 7: Streamlines of the stationary flow in one quadrant. The streamline is obtained from the first order approximation. The radius of the cylinder $a=0.11\text{cm}$ and the radius of the outer boundary $R=20*a$. [1]

Here $R_0 = a\left(\frac{\omega}{\eta}\right)^{\frac{1}{2}} = 10$. Holtmark draws an important conclusion based on his theoretical and semi-numerical analysis. As we can see from the above figure, the core of the inner vortex is located at $1 < \frac{r}{a} < 2$ (Figure 7). In a limited space, the third core can also be obtained, but for infinite space, the calculation shows that the core for outer vortex will move to infinity together with the outer boundary. The removing of the outer boundary is seen to have a negligible influence on the velocities in the inner system and on the thickness of it. The thickness of the inner vortex system is, however, compressed as $D\left(\frac{\omega}{\eta}\right)^{1/2}$ increases.

After Holtmark, Wang *et al.* [14] studied the boundary-induced type streaming under low Reynolds number and high oscillating frequency flow. In his analysis, he broke down the variables in a steady and an unsteady parts and divided the study into different

regions based on different Reynolds numbers and Strouhal numbers, $S = l\omega/U_\infty$, which is used to characterize frequency. l is a characteristic length of the body, ω is frequency of oscillation and ν is kinematic viscosity. His theory also obtained the same result as Holtsmark. The thickness of the recirculating flow depends on $D(\frac{\omega}{\eta})^{1/2}$. Bertelsen *et al.* [15] also has new numerical analysis and experiments to prove Holtsmark's result.

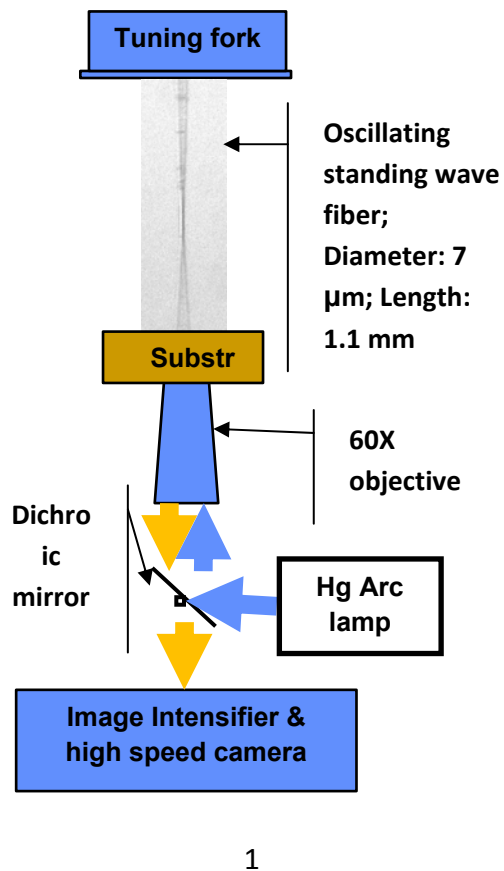
In recent years, there has been less theoretical work on steady streaming. Riley has summarized a lot of this work [16], [17] based on the discoveries of previous people.

3. Experimental Setup and Procedure

In our experiment, we measured the steady streaming flow field induced by high-frequency oscillation (32 kHz). The flow field is small ($\sim 100\mu m$) and it has a very strong 3-D motion. The objective of this experiment is trying to investigate the 3-D flow field and explore the possibility of using this technique for mixing in micro-scale.

3.1 The overall setup

The below figure shows the overall set up of this experiment. One end of a carbon fiber is put in a small amount of fluid and the other end is attached to a tuning fork (probe amplifier) which is oscillating at 32kHz, so the whole fiber and tuning fork are oscillating at 32k Hz. The glass used to hold the fluid is placed above a 60X Nikon objective. The image/video taking system consists of an image intensifier and a high speed camera (Figure 8). The high speed camera can take images up to 70,000 frames per second with a Region of Interest (ROI) of 128×128, and 5000 frames per second with full resolution 1024×1024.



2



3

Figure 8: Experimental setup 1, tuning fork, oscillating fiber, microscopy and video/image taking system. 2, Photron APX RS high speed camera. 3, Nikon TE200 inverted fluorescence microscopy.

3.2 Mechanical design

The mechanical part of the system is as shown below. Because of the very small field of view (60X objective) and the small travel range of the nano stage, a carefully measured mechanical design is needed (Figure 9), (Figure 10) in order to make sure the fiber can be positioned right above the objective and within the travel range of the nano stage.

The goniometer adjusts the inclination with a fiber. It is hard to tell the fiber inclination to naked eye. In order to do so, the objective is moved up and down. If the tip position does not move, then the fiber is vertically placed (Figure 13).

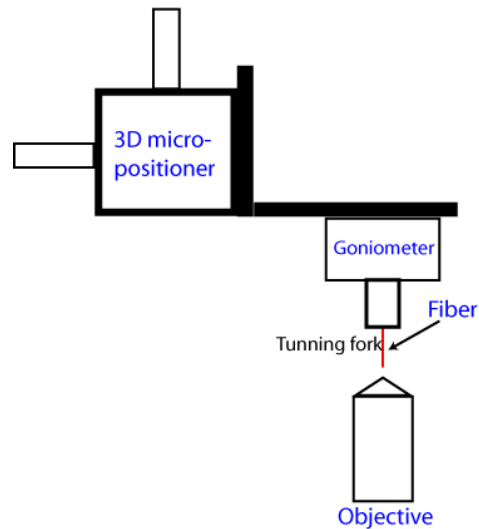


Figure 9: The “Quater Research and Development” micropositioner has a resolution of 0.01 mm per marking on the micrometers and travel range 0.5” on X, Y, Z directions. The “Thorlab” goniometer has a resolution of 0.167° and ranges of $\pm 15^\circ$ and $\pm 10^\circ$ at two rotational axes respectively. The micropositioner is used to move stage in X-, Y- and Z- directions and goniometer is used to make sure the probe (fiber) is vertically placed.

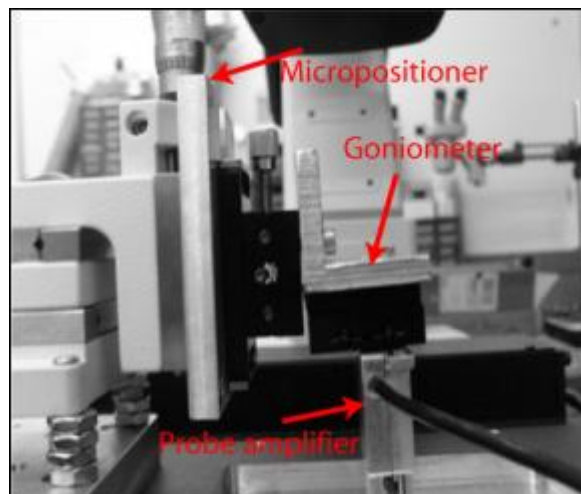


Figure 10: The front view of goniometer setup. The whole setup is placed on the micro stage of microscopy. The micro stage itself can move too.

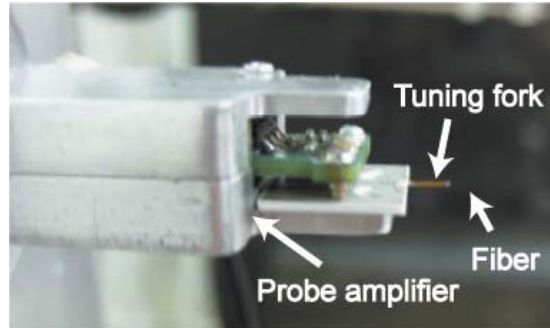


Figure 11: Oscillating fiber and its driven system. The fiber is attached to a tuning fork which is controlled by the probe amplifier and oscillates at 32 kHz.

The tuning fork, fiber, probe amplifier and control box (which are not shown in Figure 11) are provided by Insitutech, Inc. Because the fiber is tiny (1mm in length and $7\mu\text{m}$ in diameter), an appropriate mechanical setup is needed to make sure the fiber can be appropriately placed above the substrate and objective. Both the tuning fork and fiber are oscillating, but only the fiber is inserted in the fluid. If the tuning fork gets in touch with the fluid, a short circuit may result.

More importantly, the fiber is not just simply oscillating back and forth, but is vibrating as a standing wave (see Figure 12). Together with the boundary layer (the substrate beneath the tip), this causes the flow in our experiment to have a strong 3-D motion, significantly different from the work done by previous people.

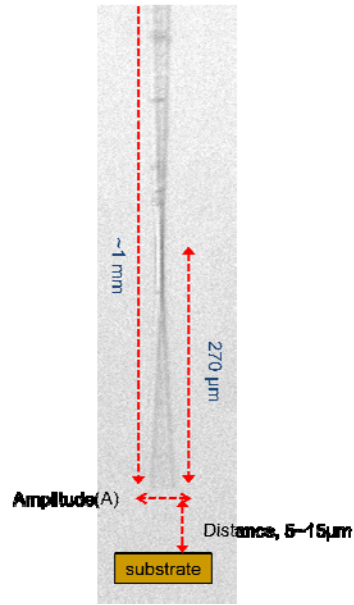


Figure 12: The actual image of standing wave fiber. The total length is 1 mm and the distance from the tip to the first node is $270\ \mu\text{m}$.

The first node of the standing wave fiber (probe) is $270\ \mu\text{m}$ away from the tip. Although most of the fiber is immersed in fluid, we are only able to see a small part of the motion ($50\ \mu\text{m}$ above the substrate) through the microscope, because of the optical limit of the 60X objective.

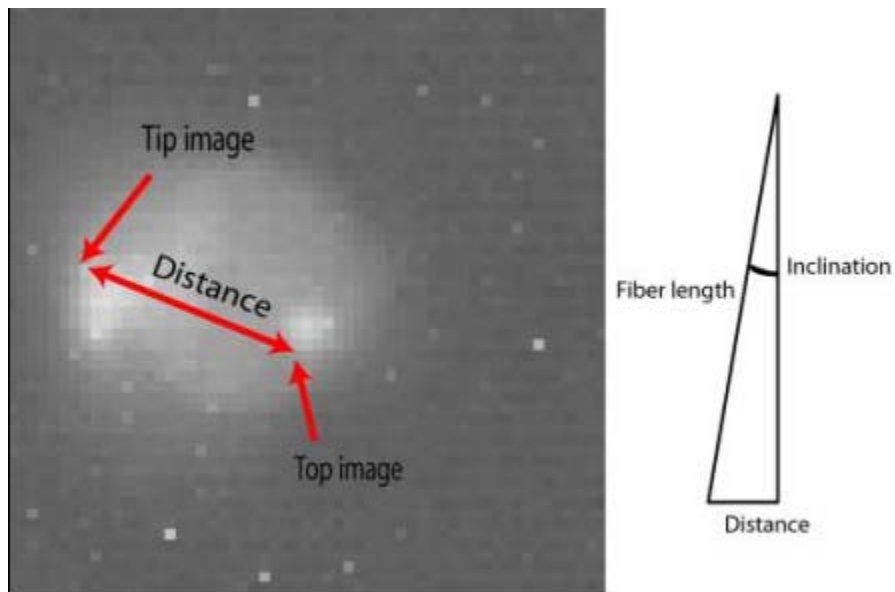


Figure 13: Adjust tip inclination. Image of the tip and the top are overlapped in one image. If we know the length of fiber, we are able to calculate the inclination angle.

3.3 Control system

The control system is a key part in synchronizing the high speed camera, image intensifier and the micro motor that control the Z-direction objective movement. Once a trigger signal is sent by the programmed NIDAQ card, the objective will move to the designated position. Then the image intensifier is turned on and finally the camera starts to record image/video (Figure 14).

In the image intensifier, the electric potential gradient between the photocathode and the MCP screen determines the exposure. We can control the shutter and exposure time through a function generator. The function generator is controlled by Matlab code.

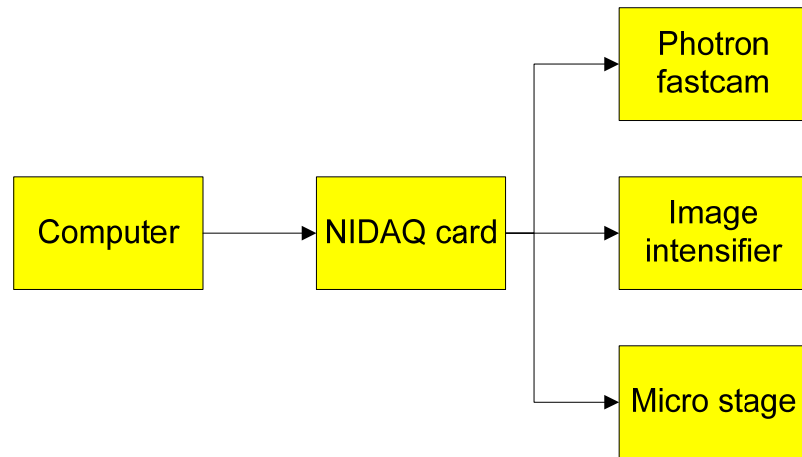


Figure 14: Schematic of the control system. Fast camera, image intensifier and micro stage are all connected to computer via NIDAQ card. They can be all controlled by a single Matlab file, which reduces a large amount of manual work.

3.4 Particle Tracking Velocimetry (PTV)

3.4.1 Advantages of PTV

Currently, micro-PIV techniques have been widely used to explore flow phenomenon in small scales. For instance, most of the inkjet printers consist of an array of nozzles with exit orifices on the order of tens of microns in diameter. The biomedical industry is currently developing and using micro fabricated fluidic devices for patient diagnosis, patient monitoring and drug delivery [18]. Micro-PIV setup usually consists of a high-resolution camera, an epi-fluorescent microscope equipped with color filters, seeding particles with a fluorescence dye and a light source (Mercury lamp for low illumination or laser. Hg lamp is used when only low illumination is required). With almost the same equipment, we used Particle Tracking Velocimetry (PTV) instead of PIV. The reasons as follows:

1. PIV usually requires a high density of seeding particles for cross-correlation purposes. Light emitted out of the focused particles reduces the signal-to-noise ratio in all the images. In our experiment, we have to penetrate the focal plane into the flow, up to $24\mu\text{m}$ from the substrate. Taking this into consideration, PTV is a suitable technique and algorithm as it requires fewer particles than PIV. Also, as PTV tracks individual particles along its path line, the algorithm identifies particles within certain radii in the previous or next frame as the identical particle in the current frame. If there are too many particles around one target particle, it increases the tracking uncertainties.

- PIV detects the shifting of flow patterns and uses cross-correlation to calculate the displacement and velocities. It requires a stable background noise during the image/video taking period. In our microscopy system, the mercury lamp intensity has a certain degree of fluctuation. This is not a serious problem in PTV because PTV tracks single particles.

3.4.2 Principles of PTV

Figure 15 shows a simple illustration of PTV principles.

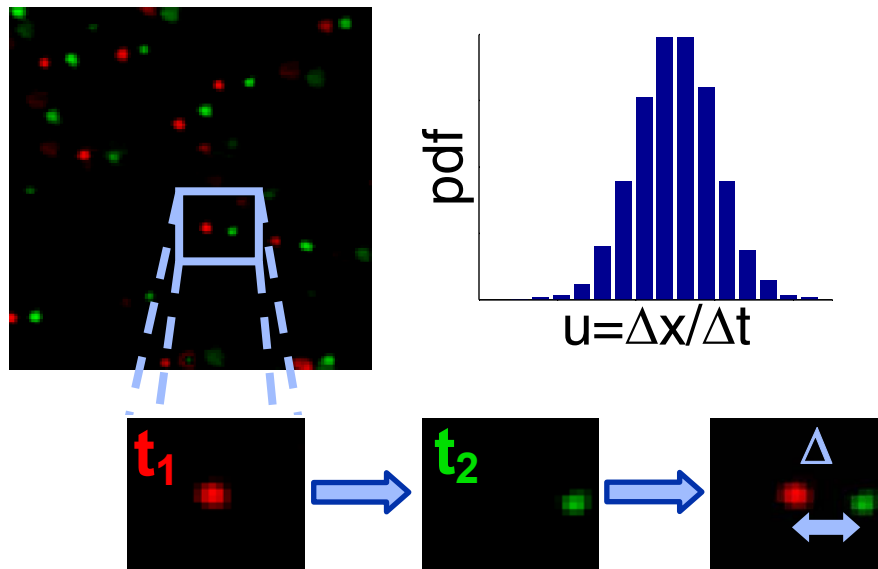


Figure 15: Basic principles of PTV. The velocity (speed and direction) is obtained by dividing the distance between two identified particles in two subsequent frames by the time interval between the frames.

PTV tracks and identifies the location (center) of individual particles across several frames, and uses the time difference between each frame to calculate the velocity

vector of each particle. The principles of identifying and correlating particles in the previous and next frame are stated below:

1. The closest (nearest-neighbor) principle. We define a “displacement threshold”. Within this threshold, all the particles have the possibility of being the same particle in the previous or next frame.
2. The minimum acceleration principle. We identify the length of displacement and direction of movement for each particle in the previous frame. Particles in the following frame which fall out of the predefined circle are judged as different particles.

If there is more than one particle identified after applying the above principles, the code will skip this particle and process others.

A typical PTV image is shown in Figure 16. The black spot in the PTV image is the fiber tip. The typical PIV image requires at least 3-4 particles in a 16×16 pixel window. For a 1024×1024 image usually consists more than 1000 particles, which will overwhelmed our flow field.

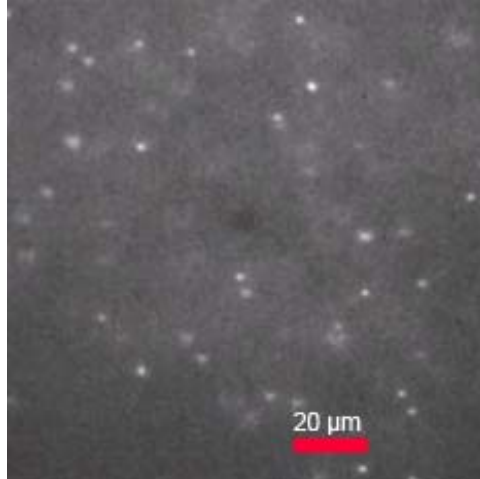


Figure 16: Comparison of PIV and PTV images. This is an ideal PTV image taken by our experimental setup. The distance among each particle is larger than its displacement between two frames. Also the particle light intensity is strong contrast to the background. They can be easily identified.

3.4.3 Choose seed particles

There are different sizes of particles we can use. They range from several nano meters (quantum dots) to several micrometers (fluorescent polystyrene). In order to achieve micro scale spatial resolution, the particles chosen are small enough to follow the flow faithfully without (1) disrupting the flow field, (2) clogging the microdevice by accumulation (3) producing unnecessarily large images. At the same time, the particles chosen must be large enough so that they scatter sufficient light to be detected [19]. For the material of particles, polystyrene is widely used because it has similar density to water ($\rho_p = 1.055$) and can be dyed by fluorescence.

If the particle diameter is smaller than the wavelength of illumination light, normal elastic scattering techniques will not work quite well. Since all the tracing particles we use are fluorescent, fluorescent excitation makes the sub micron imaging possible.

We now evaluate the diffusion effect of a $1\mu m$ particle due to Brownian motion. The following function is for a first order estimate relative to the displacement in the x-direction. [20]

$$\varepsilon_B = \frac{\langle S^2 \rangle^{1/2}}{\Delta x} = \frac{1}{u} \sqrt{\frac{2D}{\Delta t}} \quad (11)$$

Here S^2 is the random mean square particle displacement associated with Brownian motion, D is the Brownian diffusion coefficient, u is the characteristic velocity, and Δt is the time interval between pulses. If we use a $1\mu m$ size particle, 1500 frames per second and $u = 500\mu m/s$, ε_B is about 10%. Because Brownian motion is unbiased, it can be substantially reduced by averaging over several particle images.

In our experiment, we use $1\mu m$ diameter fluorescent particles because they offer adequate resolution and faithfully follow the flow outside the inner vortex (particle following the inner vortex flow is not possible due to 32 KHz oscillating frequency).

Figure 17 depicts the function (normal distribution) we use to detect the particle center.

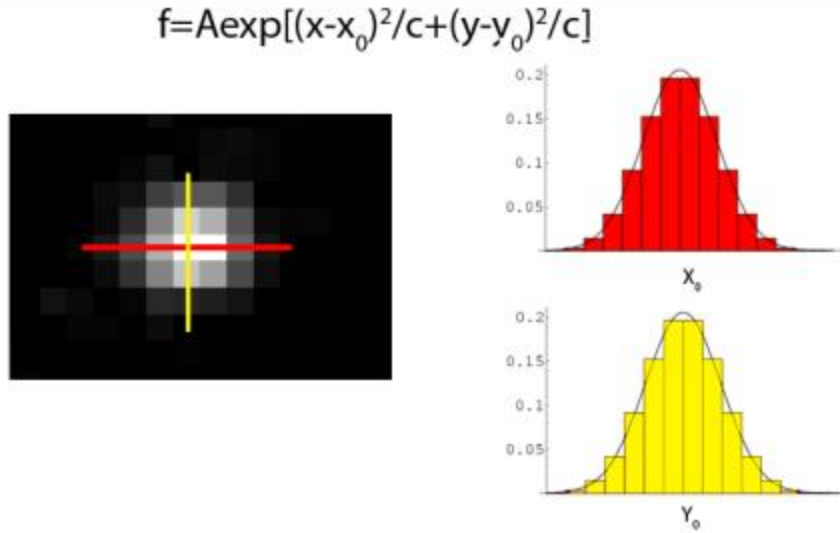


Figure 17: Particle center locating principle. Through Gaussian fit at X and Y axis, we identify the center (X_0 and Y_0) of particle with sub micron precision. The distribution shown in the figure is the theoretical intensity distribution. A is a constant here.

3.4.4 Tracking uncertainties

Brownian motion and imaging artifacts play a small role in the measurement uncertainties because of the use of $1\mu m$ size particles, which not only limit the diffusivity but also increase the particle light intensity as we have discussed above.

For Micro PTV, the spatial resolution is limited by the effective diameter of particle images when projected back into the flow field. For magnification larger than unity, the diameter of the diffraction-limited point spread function, in the image plane, it is given by

$$d_s = [2.44(1 + M_0)f^\# \lambda]^2 \quad (12)$$

where $f^\# = \frac{1}{2NA} = 0.36$ and NA is the numerical aperture of the lens. $\lambda = 510nm$ is the wavelength of the recording light. $M_0 = 60$ is the magnification of the Nikon oil

immersion objective. So $d_s=0.14\mu m$ The actual image recorded is the convolution of the diffraction-limited image with the geometric image [21]. Approximating both the geometric images and the diameter d_e of the diffraction-limited particle image, the resulting effective particle diameter d_e^2 , where

$$d_e^2 = M_0^2 d_p^2 + d_s^2 \quad (13)$$

The tracer particle diameter is $d_p = 1\mu m$. So the effective particle diameter projected onto the CCD camera is $d_e = 65.9\mu m$. The effective particle diameter when projected back into the flow is $1.09\mu m$. According to Prasad [22], if a particle image diameter is resolved by 3-4 pixels, the location of a particle-image correlation peak can be determined to within 1/10th the particle-image diameter. This yields a measurement uncertainty of $\delta_x = 109nm$.

From the above analysis, we can see that by resolving the image with 3-4 pixels across the image diameter, one can determine particle position to within an order of magnitude better resolution than the diffraction-limited resolution of the microscope.

3.5 Experiment procedure and data summarized

In order to observe the three dimensional movement of particles, the objective should be able to move up and down based on the need of our observation depth in the fluid. The working distance of the 60X objective is $200\mu m$. But as we have mentioned in section 3.4.1, because of the volume illumination, the light emitted by the out of focused fluorescent particles blurs the contrast between tracking particles and the surrounding. This limits the particle density as well as the observation depth. The

maximum observation depth is $50\mu m$ in our experiment. The memory of the Photron camera is only 2GB. It can store up 90,000 images with resolution of $256*256$. If we move up the objective $3\mu m$ each time, we can record flow information up to $24\mu m$. Although our system has limited capability in observing the flow field, but this $24\mu m$ depth gives us enough information to analyze the flow characteristics.

The following tables show all the data collected so far. In order to have flow with different Reynolds numbers, we can either change the viscosity of the fluid or the amplitude of the tip oscillation. The distance between the tip and substrate can be changed too.

Tip above substrate $10\mu m$						
	Material	Solution	Amplitude	Vrms	$\omega A^2/\eta$	$a(\omega/\eta)^{\frac{1}{2}}$
1	Carbon	74.5% glycerol	0.7	2	0.007	0.02
2	Carbon	65% glycerol	0.7	1	0.013	0.04
3	Glass	34% glycerol	0.7	0.5	0.07	0.08
4	Carbon	34% glycerol	1.11	1	0.12	0.12
5	Carbon	Water	1.38	0.5	0.31	0.25
6	Glass	34% glycerol	5.03	2.9	0.54	0.55
7	Carbon	Water	5.47	1	1.23	0.98
8	Carbon	Water	10.15	1.5	2.27	1.82
9	Carbon	Water	14.74	2	3.30	2.64

Tip above substrate $5\mu m$					
Material	Solution	Amplitude	Vrms	$\omega A^2/\eta$	$D(\omega/\eta)^{\frac{1}{2}}$
Carbon	Water	1.38	0.5	0.31	0.25
Carbon	Water	5.47	1	1.23	0.98

Tip above substrate $10\mu m$, 30° inclined					
Material	Solution	Amplitude	Vrms	$\omega A^2/\eta$	$D(\omega/\eta)^{\frac{1}{2}}$
Carbon	Water	5.47	1	1.23	0.98

PUMP						
Description	Particles at each layer become less significant after long time					
Distance	Solution	Amplitude	Vrms	$\omega A^2/\eta$	$D(\omega/\eta)^{\frac{1}{2}}$	NOTE
10	Water	5.47	1	1.23	0.98	Images before and after pumping
20	Water	5.47	1	1.23	0.98	Images before and after pumping

PUMP						
Description	An obstacle presenting, particle transferred to the other side					
Distance	Solution	Amplitude	Vrms	$\omega A^2/\eta$	$D(\omega/\eta)^{\frac{1}{2}}$	Process
10	65% glycerol	0.7	1	0.013	0.04	done

Table 1: Summarization of all the experimental data, $Re = \frac{\omega A^2}{\eta}$ or $Re = D\left(\frac{\omega}{\eta}\right)^{\frac{1}{2}}$

ω is the frequency, A is the amplitude and η is the kinematic viscosity. V_{rms} is the root-mean-square of the driven voltage. Both Re can be used to describe flow field.

According to existing literatures, $Re = D\left(\frac{\omega}{\eta}\right)^{\frac{1}{2}}$ has been used more frequently. All the

Reynolds number described followed are all referred to $Re = D\left(\frac{\omega}{\eta}\right)^{\frac{1}{2}}$ if not otherwise

stated.

4. Results and discussion

4.1 Calibration

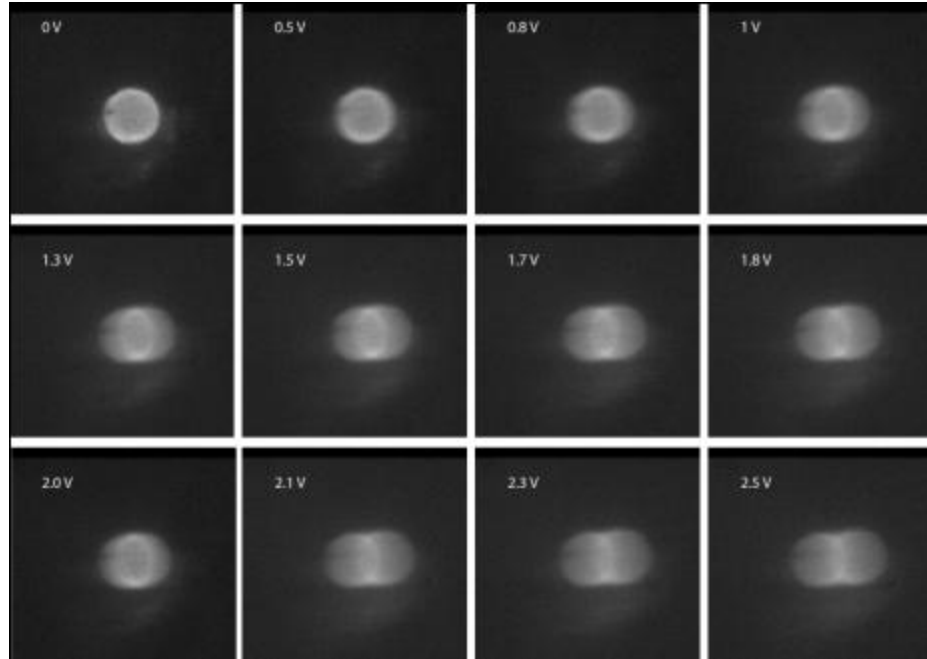


Figure 18: Tip oscillating images in water. The fiber material is glass and the solution is water. Driven voltage starts from 0V to 2.5V. Images are taken by IDT camera.

The series of images (Figure 18) show the tip of a glass fiber oscillating in the water. The Dichroic mirror in the microscope's light path can only allow emitted fluorescent light to pass. The reason we can see the tip moving is that its surface is coated with rhodamine solution. Also the oscillating frequency is high enough (32 KHz) that many oscillation cycles can be seen, within the set exposure time. That is why we can get a clear image of the oscillating amplitude. The camera is an IDT camera with sensor of $7\mu\text{m}$ pixels size, a significant improvement from the Photron (fast speed) camera ($17\mu\text{m}$).

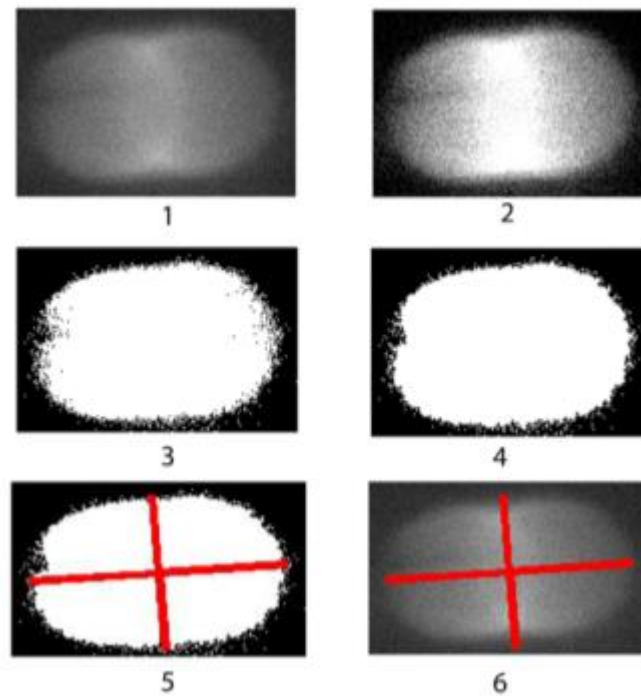


Figure 19: Image processing for tip amplitude.

(1), crop the region of interest from the original image; (2), saturate the lowest and highest 10% of pixels in the image; (3), calculate a threshold and binarize the image; (4), fill in the black gaps surrounded by white pixels; (5), calculate the major axis of the ellipse that has the same normalized second central moments as the region; (6), Plot the long axis and short axis on the original image. The reasons we are trying to measure oscillation amplitude by the above mentioned steps are because the first intensity is gradually decaying from the tip center to the fluid. There is no sharp edge telling us where the end motion of the tip is. The second is that amplitude will tend to be very small when the driven voltage is low and viscosity of fluid is high. In this situation, it is very inaccurate to measure by eye. From the 6th plot in the above image, we can see the

measured long axis and short axis fit the original image very well. It gives a high confidence in measuring the amplitude.

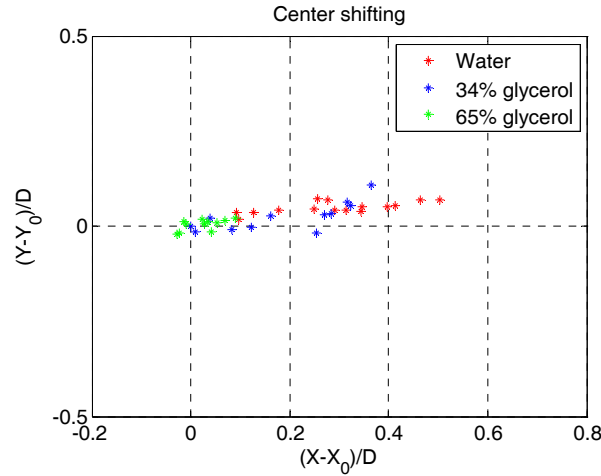


Figure 20: Tip oscillating center shifts as the amplitude increases. D is the tip diameter and Y_0, X_0 are the beginning locations.

From Figure 20, we can see the shifting is mostly limited on the X-axis, with which the tip is oscillating. It has little or no motion on the Y-axis. It is interesting that the tip center moves in the same direction (positive X-axis) when the amplitude increases. The shifting is smaller for higher viscosity as the oscillation is damped by the viscosity.

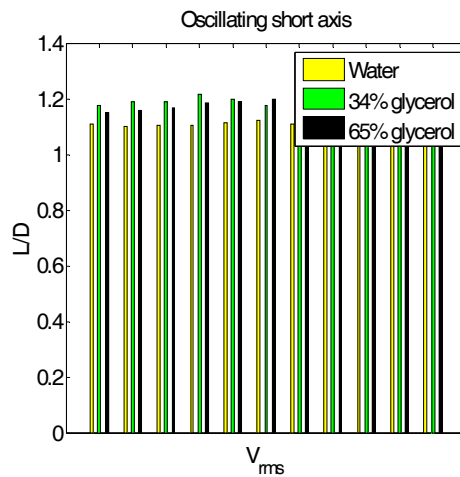


Figure 21: Length of short axis vs. driven voltage. D is the tip diameter and L is the actual length of short axis.

The short axis should be the same as tip diameter if the movement is just on the X-axis (Figure 21). From the above figure, we are very confident in saying that the tip is moving in a straight line on X-axis.

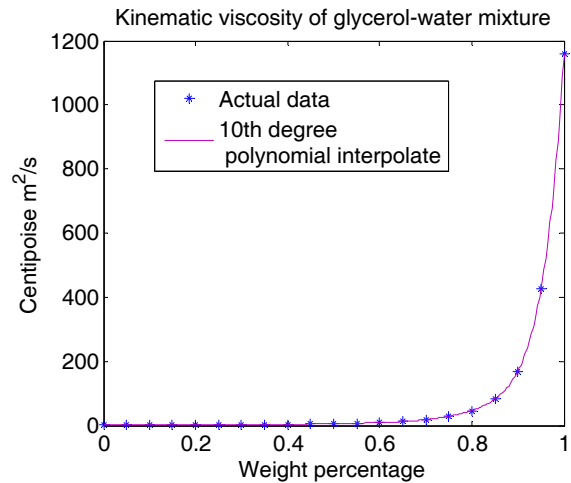


Figure 22: Viscosity of water and glycerol solution. X-axis is the weight percentage of glycerol in solution.

Because it is not possible to determine the kinematic viscosity of specific glycerol and water mixture, we interpolated the data give by Archbutt [23] and Shankar [24]. The 10th degree polynomial interpolation (Figure 22) fits the data very well.

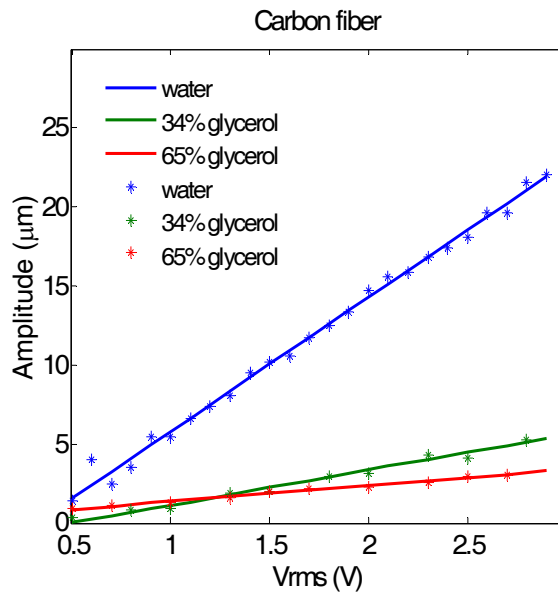
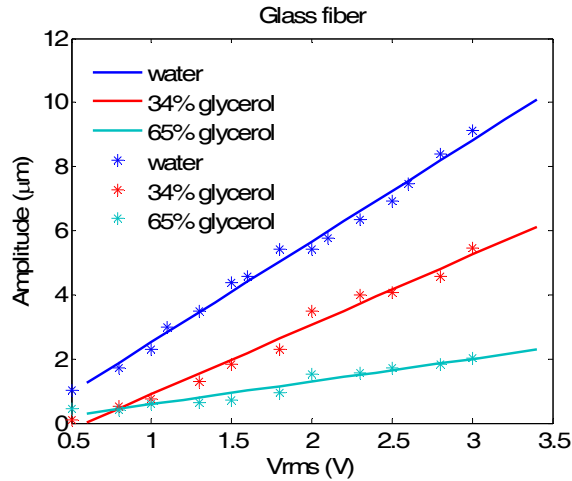


Figure 23: Amplitude vs. driven voltage. Blue, red and green means water, 34% glycerol and 65% glycerol solution respectively. V_{rms} means the root mean square velocity. Under different percentage of glycerol and water mixture, the amplitude changes significantly. But they all remain linear.

For both the glass and carbon fibers, their amplitudes change linearly with the driven voltage (Figure 23). For the glass fiber, amplitudes decrease gradually with viscosity changes. But for the carbon fiber, its amplitude decreases sharply, between water and

34% glycerol. The slope also decreases as the viscosity of fluid increases, which means the damping confines the tip movement.

4.2 2-D Flow field

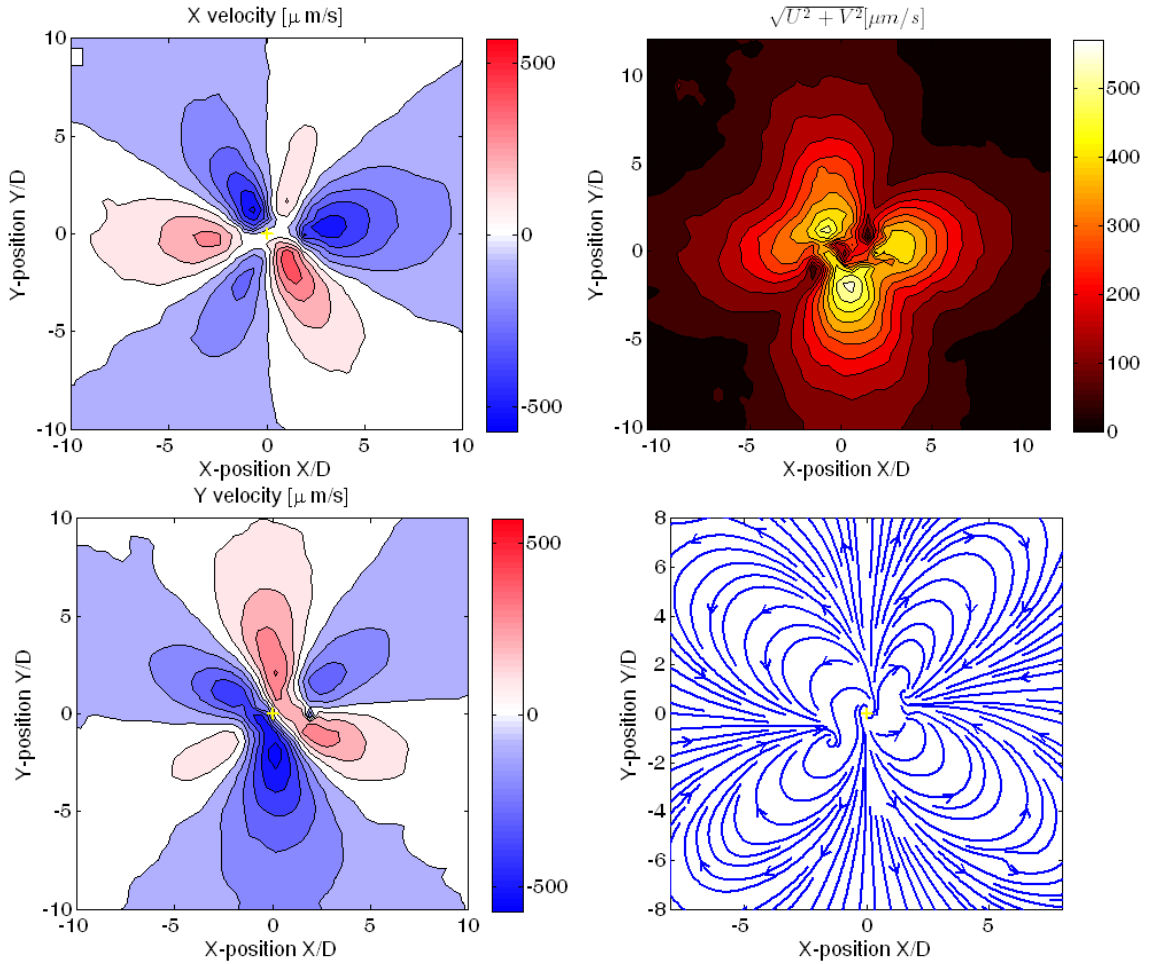


Figure 24: video processing results--Streamlines and contours for horizontal velocities.

The tip is placed $10\mu\text{m}$ above the substrate, oscillating along X-axis with $1.38\mu\text{m}$ amplitude. The Reynolds number is 0.25. Red means flow goes to the positive side of the axis and blue means flow goes to the negative side of the axis.

From Figure 24, we can see the tip is oscillating along the X-axis. The flow comes into the center along the X-axis and goes out the center along the Y-axis. The horizontal streamlines do not show the actual path line of seed particles, because the flow is three dimensional. All the horizontal motion of particles form into four eddies adjacent to the oscillating center. The results are very similar to the 2-D experiments people have done before [9]. Four eddies are formed by Reynolds stress which comes from viscosity of the fluid and non linearity of the inertial effect. The horizontal speed gradually decays from the center where we can see the symmetry and gradual decay in the contour. The tracking uncertainties (standard deviation of velocity vectors) are kept below 5% at all the locations. The amplitude of tip oscillation is $1.38\mu\text{m}$ and the whole velocity field has a radius of about $60\mu\text{m}$.

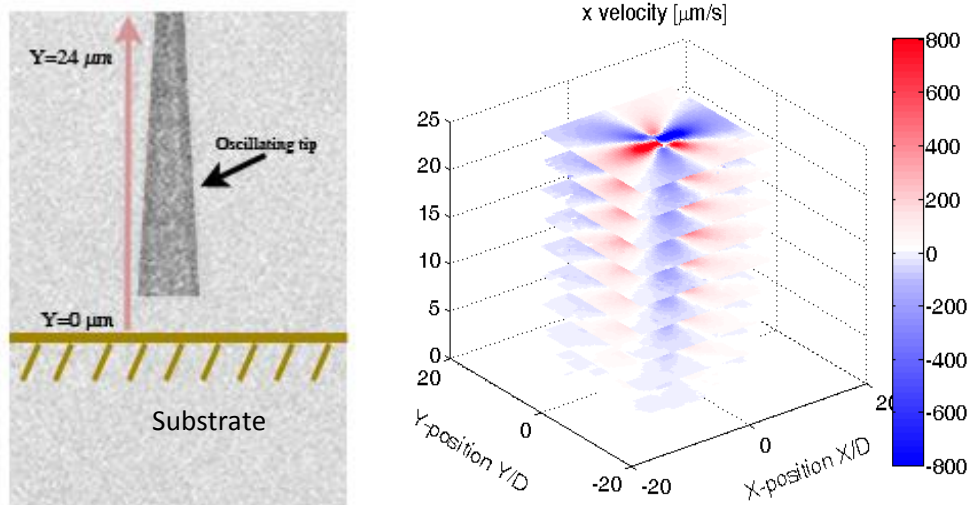


Figure 25: Processing images of different flow layers. The left one shows how focal plane moves up by $3\mu\text{m}$ each time and records videos. The right one quantitatively shows the image processing results of multi-layer video recording and tells us how the horizontal velocities increase from the substrate. ($Re=0.25$)

One of the major differences of our experiment compared with previous people is our accurate measurement of the flow field not just in one 2-D plane but several 2-D planes. But this multi-layer measurement (Figure 25) has its own limit. As shown in the previous chapter, the total length of fiber is larger than $1mm$, which is much larger than $24\mu m$, the largest depth we penetrate into the flow field. What we are capturing here is a very small region of the whole 3-D flow field, and it is far below the first node ($h=270\mu m$). The amplitude changes roughly linearly from tip to node. So we know if the amplitude at the tip is D , the amplitude $14\mu m$ above the tip ($24\mu m$ above substrate) will be $0.95D$. From the observed regions ($h=0\mu m \rightarrow h=24\mu m$), the velocity keeps increasing as evidenced by the color become darker in the contour plots. Thus, we think the flow is more influenced by the boundary (substrate) than the difference of the amplitude.

4.3 3-D Flow field

$$\frac{\partial U}{\partial x} + \frac{\partial V}{\partial y} + \frac{\partial W}{\partial z} = 0 \quad (14)$$

$$W = \int_0^h -\left(\frac{\partial U}{\partial x} + \frac{\partial V}{\partial y}\right) dz \quad (15)$$

Once all the PTV data are obtained at different heights, we have the information of horizontal velocities (U and V) at different heights. If we assume incompressible and steady flow, based on the continuity equations shown above, velocity along the Z-axis (W) can be reconstructed. Here we use a no-slip boundary to define the boundary condition at the substrate and Simpson's rule of integration with an interval of $3\mu m$ for each step.

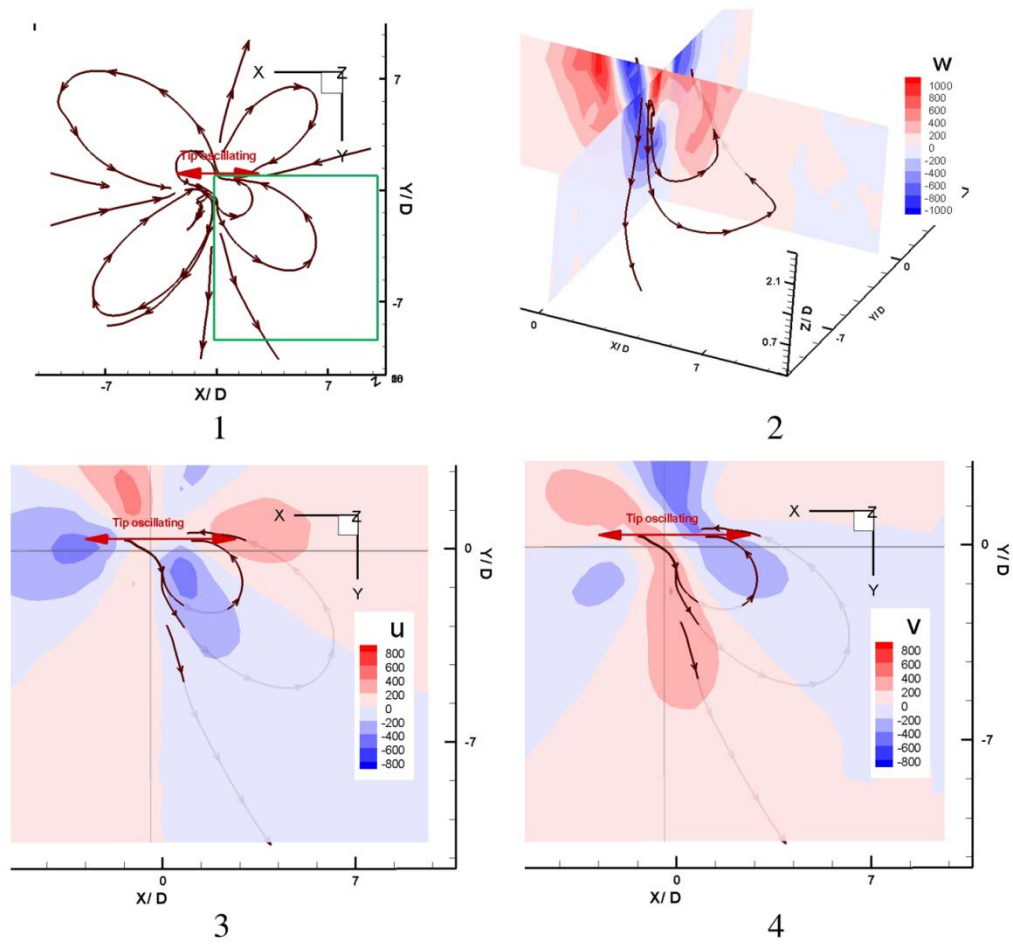


Figure 26: 3-D streamlines. (1), top view, the streamlines in the green rectangular box is shown in 3-D in the rest of the plots; (2), 3-D view of streamlines and W velocity contour; (3), U velocity contour; (4), V velocity contour. ($Re=0.25$)

The 3-D reconstruction results (Figure 26) not only show qualitative but also quantitative Z-axis motion. The first one shows the top view of streamlines ($Re=0.25$). The rest show the streamlines and contours of the region within the green square box in the first one. For contours of plot 2, 3 and 4, blue means flow goes to the negative direction of the axis while red is the positive. From the streamlines and contours, we can

tell: (1), the flow converges at the center on the axis which the tip is oscillating on. (2), the flow converges at the center with upward motion, and is propelled away from the center with downward motion. (3), the Z-axis velocity is the strongest in the center. This can be also shown by watching the video. Particles quickly disappear or appear again at the center.

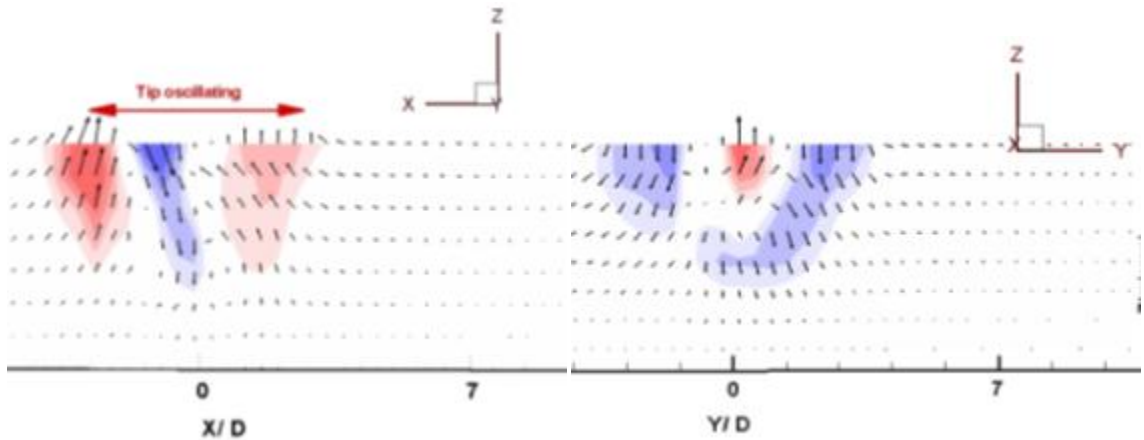


Figure 27: Velocity vector cross-section manifestation. The left one is on the plane parallel with X at $y=0$, the right one is parallel with Y at $x=0$. Red means the flow is going up and blue means the flow is going down. ($Re=0.25$)

Here we try to investigate more the velocity at the cross-plane at $X=0$ and $Y=0$, respectively (Figure 27). Blue means the flow goes to the negative side of the axis. Red means the opposite. From the above figures we can see, after the flow converges at the center, the oscillation propels the flow outwards with downward motion. This repeats during the whole recording period.

4.4 Amplitude effects

4.4.1 Energy versus Reynolds number

If we define a circle around the oscillating center and interpolate the surrounding fluid velocity onto this circle, including U, V and W. The circle has certain radius R and is placed at different heights (Figure 28). Energy is defined as $(U^2 + V^2 + W^2) \times r \times 2\pi$. D is the diameter and R is the radius of the tip.

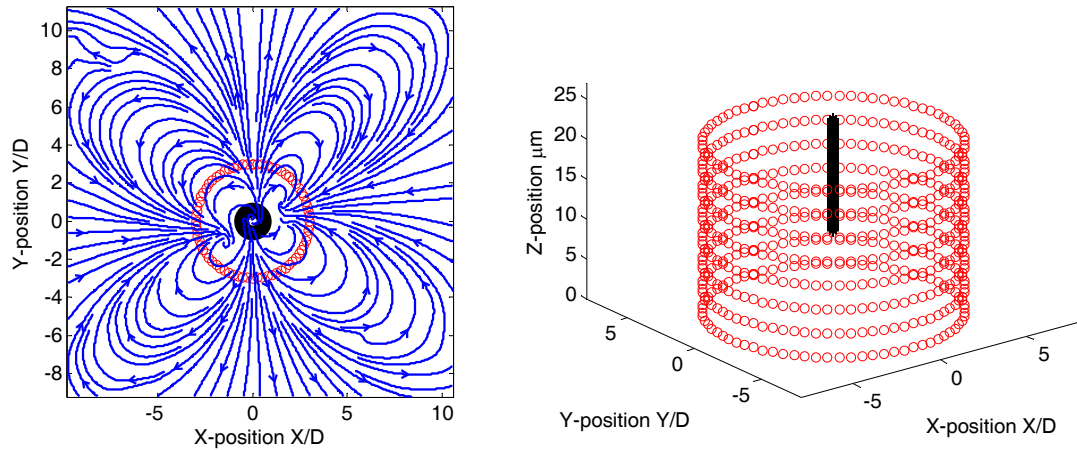


Figure 28: Calculating the energy. The red circle in left figure shows where we interpolate the surrounding fluid to get the flow field energy. The right figure tells we calculate the flow field energy at different heights.

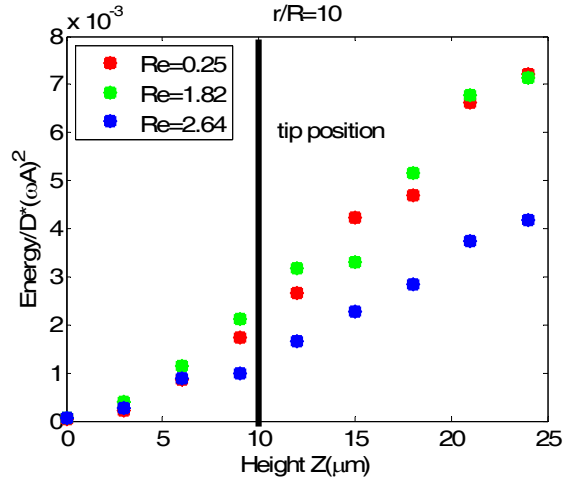


Figure 29: Energy versus height under four different Reynolds numbers.

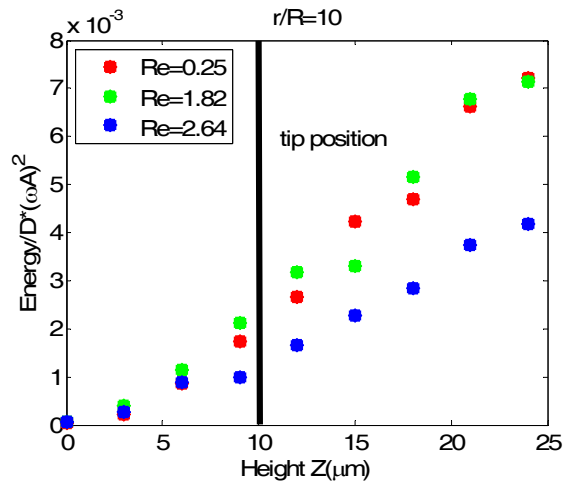


Figure 30: Normalized energy versus height under four different Reynolds numbers.

Normalized energy is defined as $Energy/D \cdot (\omega A)^2$. The energy increases as the height increases. Figure 29 shows the absolute energy and Figure 30 normalizes it with tip oscillation energy. We speculate that at certain height, the energy will reach its maximum. Due to the limit of our optical system, we are not able to clearly see the flow field above $24\mu m$.

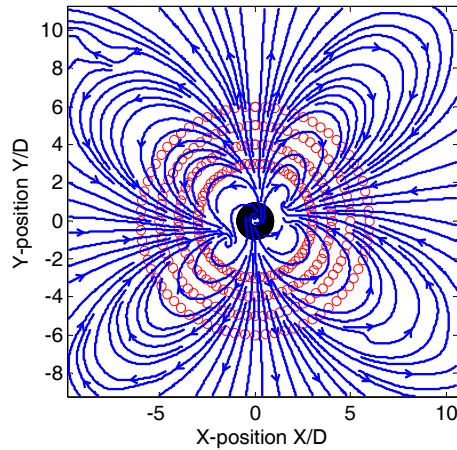


Figure 31: Energy based on different radii. We defined circles with different radii surrounding the tip. By interpolating velocities u , v and w on the circle, we can calculate the flow field energy. The black dot in the center represents the tip of the oscillating fiber.

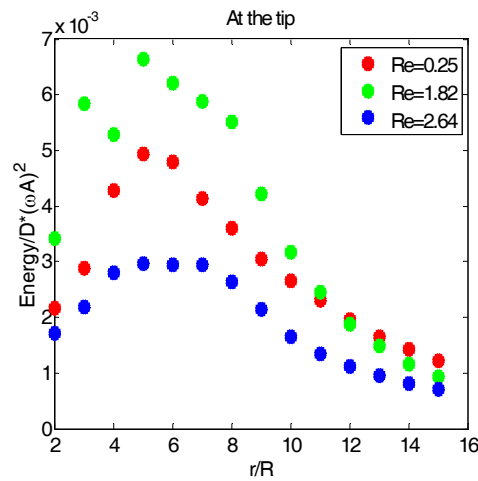


Figure 32: Energy decays from the center for four different Reynolds numbers.

As shown by Figure 32, energy is damped by viscosity. It reaches its maximum at $r/R=5$. The further away from the center that the tip oscillates, the less energy the fluid can obtain. Because the flow field is 3-D, except for knowing the total energy, we are also

interested in seeing the contribution from horizontal motion and vertical motion, respectively (Figure 33). If we break down the total energy into horizontal energy and vertical energy, we have the following plot.

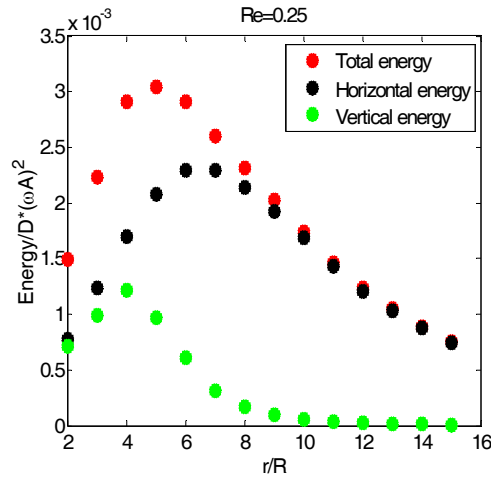


Figure 33: Horizontal energy versus vertical energy obtained at the case $Re=0.25$. It is taken at the height where the tip is. D is the diameter and R is the radius of the tip.

The horizontal energy is defined as $(U^2 + V^2) \times r \times 2\pi$ and the vertical energy is defined as $(W^2) \times r \times 2\pi$. The vertical energy reaches its maximum before horizontal energy and decays sharply after that. After $r/R = 8$, the total energy is solely due to the horizontal energy. We also want to see the total energy which is confined by a volume, such as the total energy that is included in a cylindrical volume space where the fiber is at the center.

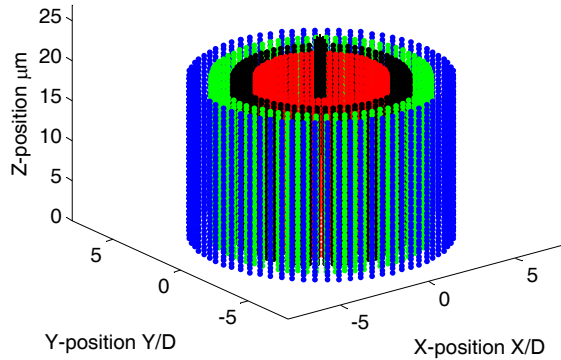


Figure 34: Energy integrated by volume. We sum all the velocities lying on the volume of the cylinder by different radii (red, black, green and dark), from the height $z=0$ to $z=24\mu m$. The cylinders radius increase from $r/D=2$ to $r/D=6$, where D is the diameter of the tip. The black column in the middle represents the fiber.

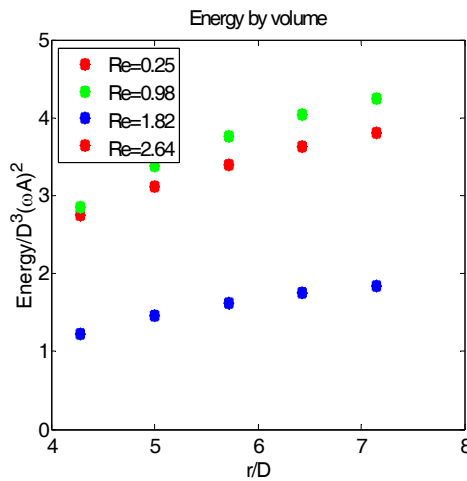


Figure 35: Energy integrated by volume.

At first, the energy integrated by volume increases as the radius increases (Figure 35). This is intuitive because the bigger the volume, the more energy it contains. Second, from the figure, the higher the Reynolds number, the more efficient the energy

transfers from the tip to the flow. Third, the linear relation tells us the energy generated by the oscillating tip distributes to the flow in a linear way.

If we only integrate the energy on the cylindrical surface where the tip is at the center as shown in Figure 34, we have the following plots. (Figure 35 is integrated by volume, and Figure 36 is integrated by surface)

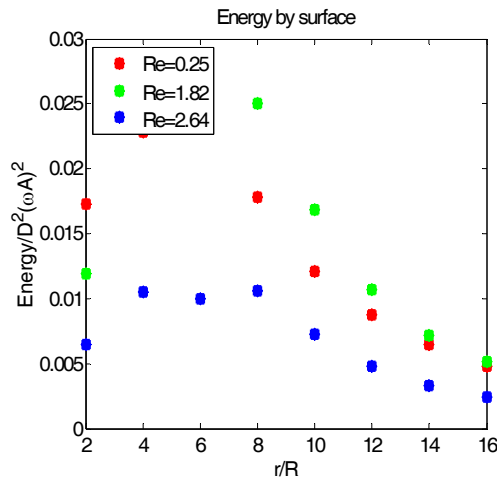


Figure 36: Results of the energy integrated on surface. The radius increases from $r/R=2$ to $r/R=12$.

As the radius increases, the energy does not drop too much until $r/R=8$. Figure 36 tells us that the energy is conserved over certain distances but viscosity finally dampens the velocity. It is interesting that the energy first increases and then decreases. We perceive the energy as low at the center because we are lacking flow field information since the camera is not able to capture such high speed motion at the tip.

4.4.2 Streamlines versus Reynolds number

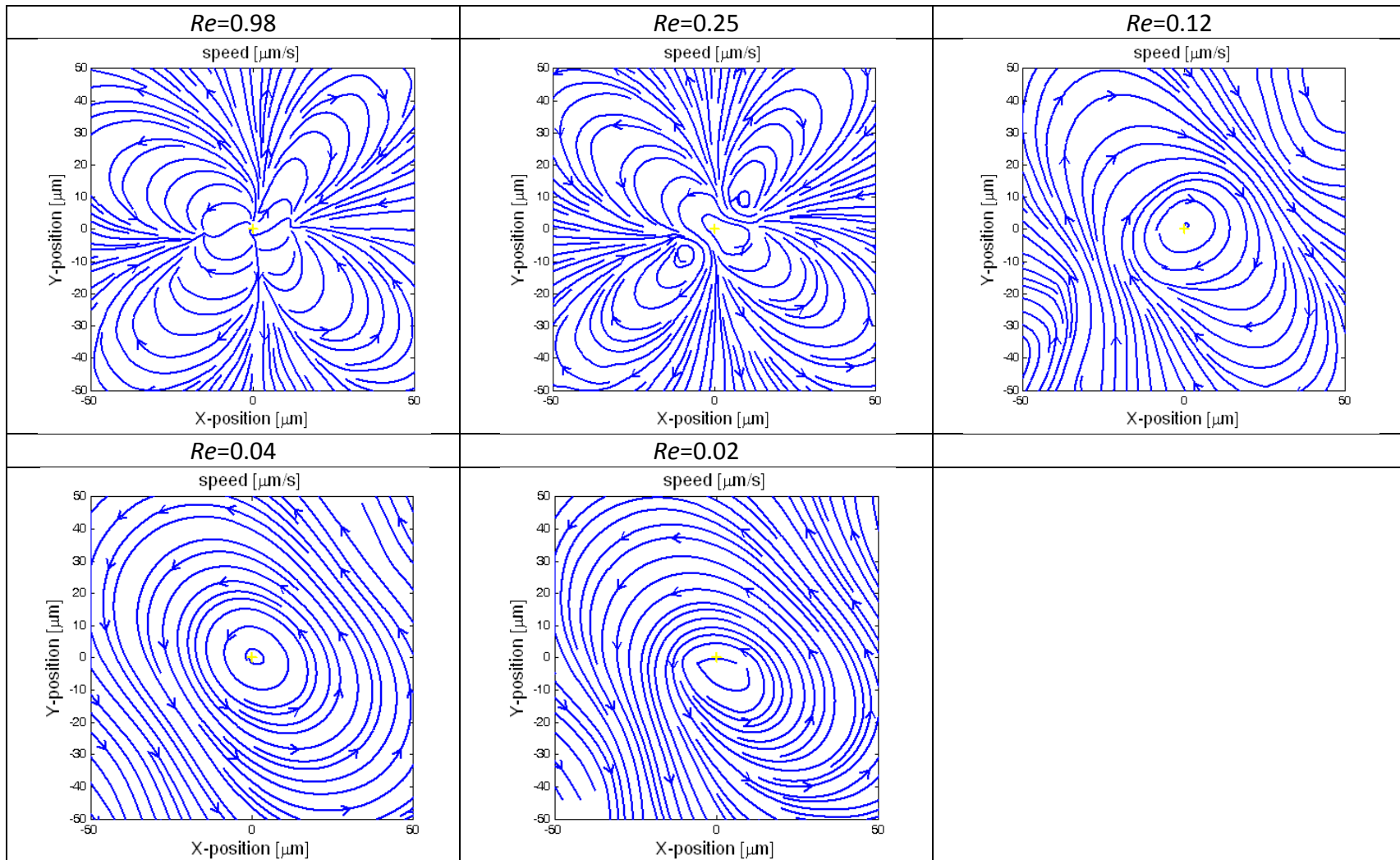
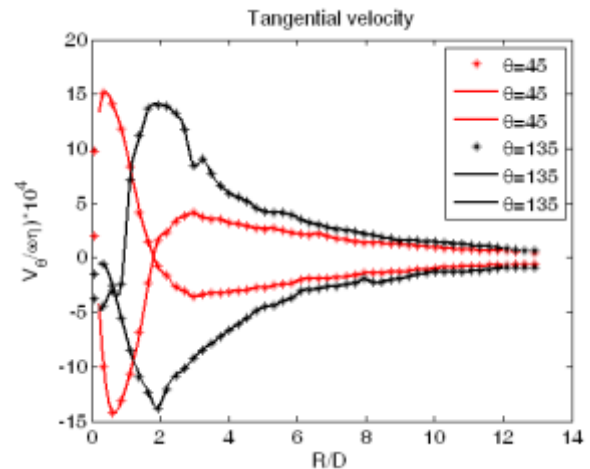
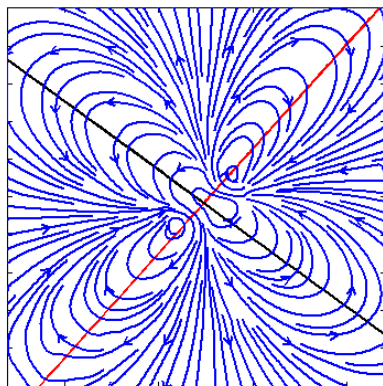


Figure 37: Flow fields transform as the Reynolds number changes.

As already shown in Table 1, we have flow fields under different Reynolds numbers. The reason why we are interested in low Re number is because in many biomedical application, we are dealing with polymers or none Newtonian fluids that have very low Re numbers. If we want to prove our device can be used to mix reagents in very small scale, we should investigate flows under low Re numbers. Although currently there is no theory of 3-D steady streaming, Wang [14] stated he stated that with a low Reynolds number (high viscosity) and high Strouhal number (high frequency), the inner

Case one



Case two

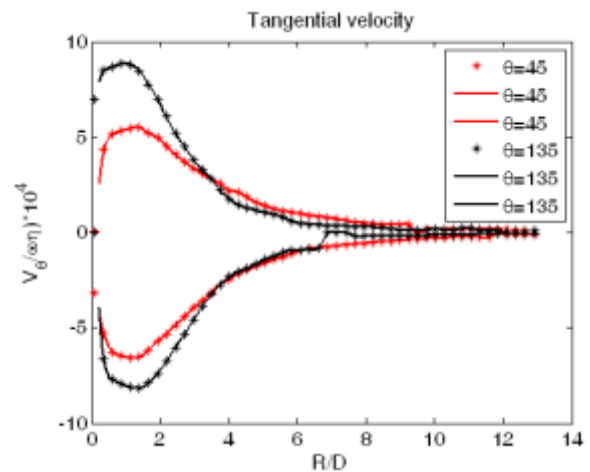
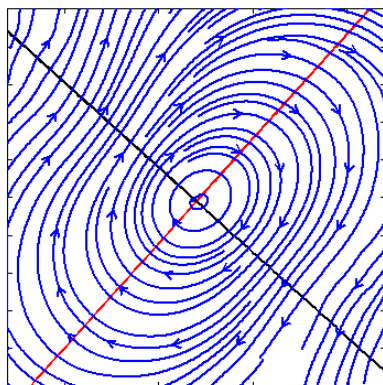


Figure 38: Tangential velocity decays along the center. Tangential velocities are interpolated on the red and black straight line. $Re=0.98$ (above). $Re=0.04$ (below).

Vortex or the unsteady vorticity would not be confined in a boundary layer but would be spread all over the flow field. Also from Holtmark [1] and Wang [14], it has been shown that the thickness of inner vortex will grow as $D\left(\frac{\omega}{\eta}\right)^{\frac{1}{2}}$ decreases. We think the previous theories can explain the phenomena here.

In Holtmark's paper [1], he stated that the second zero point where the tangential velocity curve crosses the X-axis was the core of the inner vortex. It was located between $1/2D$ and D , where D is the diameter of the tip. In the top right image of Figure 38, tangential velocities in two quadrants cross X-axis, but at different positions, so we cannot state here the zero point is the core of inner vortex. Because the tip moves back and forth very quickly and the theoretical core of the inner vortex lies between $1/2D$ and D , the tangential velocity turns around and decays very fast at $r/D=2$ in both case one and two, In case two because there is only one circulation around the tip, the tangential velocities always move in the same direction and with a smaller initial speed.

We are also interested in seeing the Z-axis motion intensity in the low Reynolds number case.

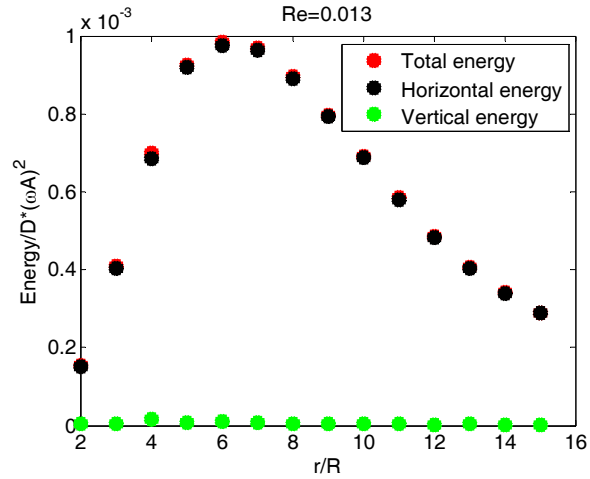


Figure 39: Energy decays from the center for the case $Re=0.04$.

So from the Figure 39 and Figure 33, we can see the vertical energy in low Re number case is much smaller compared with horizontal energy. This means that Z-axis movement is weaker than the horizontal movement.

4.4.3 Distance effect

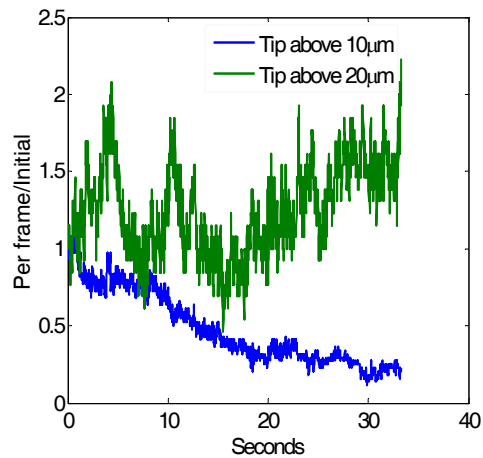


Figure 40: Pumping & boundary effect. Tip is placed above substrate $10\mu m$ or $20\mu m$. The Y-axis shows the number of particles per frame at time t divided by the number of particles at the initial frame.

When the tip is placed closer to the substrate, it has a strong pumping effect. As we can see from the blue line in Figure 40, the number of particles has been significantly decreased until it reaches a certain level. If we place the tip further away from the substrate, the pumping effect disappears (green line) as the interaction with the boundary decreases.

5. Conclusion and future study

In this thesis, we study the high speed 3-D steady streaming motion generated by an oscillating microfiber. First, we used our own optical system setup to take videos of flow fields at different heights. Second, we used our own-programmed PTV code to analyze videos and obtain velocity contours and streamlines. Third, based on the continuity equation and flow information at different heights, 3-D streamlines were reconstructed. We can understand what the 3-D motion looks like in a very intuitive way. Fourth, by looking at the flow field energy for different Reynolds numbers, different heights, different radii and by volume integral or surface integral, we are able to study the flow field energy in a quantitative way. For the horizontal plane, the energy decays as the radius increases and the vertical contribution decays much faster than the horizontal one. For the volume integral, the flow field energy stays stable but finally drops after a certain distance away from the center. Fifth, I looked at the flow field under different Reynolds numbers. The flow field changes significantly under low Re numbers. With high frequency and high viscosity, the inner vortex layer expands to the whole flow field. Thus instead of having four eddies, we have one big circulation around the center. Sixth, we studied the tangential velocity decays and found that this is similar to the 2-D cases people have previously studied. We also found out that the Z-axis fluid motion is much

smaller relative to horizontal fluid motion for a low Re number. Finally, we verified the strong influence of a boundary (substrate) by looking at the pumping effect. When the tip is further away from the substrate, the pumping effect will decrease or disappear.

So far, we have been qualitatively and quantitatively studying the flow induced by an oscillating microfiber. This is the first time that 3-D steady streaming has been studied in a quantitative way, especially in considering the flow field energy and velocity decay.

For future study, more experiments under the low Reynolds number region and the mixing effect caused by 3-D steady streaming can be studied. Mixing in microfluidic devices is still a challenge remaining to be solved.

Bibliography

1. Holtsmark, J., et al., *Boundary layer flow near a cylindrical obstacle in an oscillating, incompressible fluid*. The journal of the acoustical society of America, 1954. **26**(1).
2. Eckart, C., *Vortices and Streams Caused by Sound Waves*. Physical Review, 1948. **73**(Copyright (C) 2010 The American Physical Society): p. 68.
3. da C. Andrade, E.N., *On the Circulations Caused by the Vibration of Air in a Tube*. Proceedings of the Royal Society of London. Series A, 1931. **134**(824): p. 445-470.
4. Rife, J.C., et al., *Miniature valveless ultrasonic pumps and mixers*. Sensors and Actuators A: Physical, 2000. **86**(1-2): p. 135-140.
5. Yang, Z., et al., *Ultrasonic micromixer for microfluidic systems*. Sensors and Actuators A: Physical, 2001. **93**(3): p. 266-272.
6. Sritharan, K., et al., *Acoustic mixing at low Reynold's numbers*. Applied Physics Letters, 2006. **88**(5).
7. Squires, T.M. and S.R. Quake, *Microfluidics: Fluid physics at the nanoliter scale*. Reviews of Modern Physics, 2005. **77**(3): p. 977-1026.
8. Lutz, B.R., J. Chen, and D.T. Schwartz, *Microfluidics without microfabrication*. Proceedings of the National Academy of Sciences of the United States of America, 2003. **100**(8): p. 4395-4398.

9. Lutz, B.R., J. Chen, and D.T. Schwartz, *Microscopic steady streaming eddies created around short cylinders in a channel: Flow visualization and Stokes layer scaling*. *Physics of Fluids*, 2005. **17**(2).
10. Lin, C.M., et al., *Microvortices and recirculating flow generated by an oscillatory microplate for microfluidic applications*. *Applied Physics Letters*, 2008. **93**(13).
11. Rayleigh, J.W.S., *Scientific Papers*. Vol. 108. 1883, Teddington: Cambridge University Press.
12. Rayleigh, J.W.S., *Theory of Sound*. second ed. 1894, London: Macmillan.
13. Nyborg, W.L., *Acoustic Streaming due to Attenuated Plane Waves*. *The journal of the acoustical society of America*, 1953. **25**(1): p. 68-75.
14. Wang, C.-Y., *On high-frequency oscillatory viscous flows*. *Journal of Fluid Mechanics Digital Archive*, 1968. **32**(01): p. 55-68.
15. Bertelsen, A., et al., *Nonlinear streaming effects associated with oscillating cylinders*. *Journal of Fluid Mechanics Digital Archive*, 1973. **59**(03): p. 493-511.
16. Riley, N., *Acoustic streaming*. *Theoretical and Computational Fluid Dynamics*, 1998. **10**(1-4): p. 349-356.
17. Riley, N., *Steady streaming*. *Annual Review of Fluid Mechanics*, 2001. **33**: p. 43-65.

18. Vennemann, P., et al., *In vivo micro particle image velocimetry measurements of blood-plasma in the embryonic avian heart*. Journal of Biomechanics, 2006. **39**(7): p. 1191-1200.
19. Meinhart, C.D., S.T.Wereley, and J.G.Santiago, *PIV measurements of a microchannel flow*. Experiments in Fluids, 1999. **27**(5): p. 414-419.
20. Santiago, J.G., et al., *A particle image velocimetry system for microfluidics*. Experiments in Fluids, 1998. **25**(4): p. 316-319.
21. Keane, R.D. and R.J. Adrian, *THEORY OF CROSS-CORRELATION ANALYSIS OF PIV IMAGES*. Applied Scientific Research, 1992. **49**(3): p. 191-215.
22. Prasad, A.K., et al., *EFFECT OF RESOLUTION ON THE SPEED AND ACCURACY OF PARTICLE IMAGE VELOCIMETRY INTERROGATION*. Experiments in Fluids, 1992. **13**(2-3): p. 105-116.
23. Archbutt, Deeley, and Gerlack, *Viscosity and density of glycerol in aqueous solution at 20 celcius* 1918, National Bureur of Standards Technology.
24. Shankar, P.N. and M. Kumar, *Experimental Determination of the Kinematic Viscosity of Glycerol-Water Mixtures*. Proceedings: Mathematical and Physical Sciences, 1994. **444**(1922): p. 573-581.